Letter

P Doping Promotes the Spontaneous Visible-Light-Driven Photocatalytic Water Splitting in Isomorphic Type II GaSe/InS Heterostructure

W. X. Zhang, Y. Yin, and C. He*

Read Online

ACCESS | Metrics & More | Article Recommendations | SI Supporting Information

ABSTRACT: The development and design of clean and efficient water splitting photocatalysts is important for the current situation of energy shortage and environmental pollution. A new type of isomorphic GaSe/InS heterostructure is constructed, and the optoelectronic properties were studied through first-principles calculations. The results show that GaSe/InS vdW heterostructure is a type II semiconductor with a band gap of 2.09 eV. However, through the analysis of the energy band edge position and Gibbs free energy change of water splitting, it is found that the GaSe/InS heterostructure is difficult to undergo overall water splitting. Therefore, nonmetallic element P doping is considered, the established P-doped GaSe/InS (P-GaSe/InS) heterostructure could maintain the type II band arrangement, and under acidic conditions, P-GaSe/InS heterostructure could spontaneously undergo overall water splitting thermodynamically. Furthermore, the low exciton binding energy of P-GaSe/InS heterostructure highlights better light absorption performance. Therefore, these findings indicate that P-GaSe/InS heterostructure is a promising photocatalyst in overall water splitting.
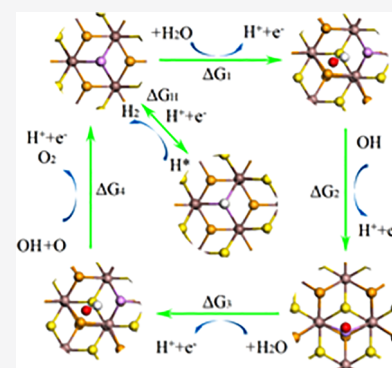
The industrial society created by human beings and the earth's ecosystem are corresponding to each other. With the depletion of traditional fossil energy, the damage to the earth's ecosystem become more and more severe. For coordinating the contradiction between energy and environment, exploring a renewable clean energy has become the top priority.[1,2] Hydrogen energy stands out because it is pollution-free, transportable, and easy to store. Hydrogen energy, which is a kind of secondary energy, has become the direction of people's efforts to extract it from water by using solar energy.[3,4] In recent decades, a large number of semiconductor materials have been explored as typical photocatalysts, such as TiO_2,[5] ZnO,[6,7] and $g\text{-}C_3N_4$.[8,9] For the semiconductor photocatalytic water splitting hydrogen production system, the electrons migrate to the surface of the catalyst in order to reduce H^+ and release H_2. At the same time, an outstanding photocatalyst needs to match the band edge position of semiconductor with the redox potential of water, have excellent adsorption to H^+, and easily desorb the generated H_2 from the catalyst surface.[10−12] Therefore, the selection of efficient semiconductor catalysts is the key factor to improve the catalytic efficiency.

The monolayer semiconductor photocatalyst has insufficient light absorption and is prone to recombination after charge separation, which severely reduces the photocatalytic efficiency.[13,14] In this regard, the idea of forming a heterostructure through the recombination of two or more semiconductors is proposed to improve the catalytic efficiency.[15,16] The

constructed $Co_9S_8/Cd/CdS$ heterostructure by Zhang et al. greatly promotes the redox activity and has a high hydrogen production rate.[17] Two-dimensional metal chalcogenides are widely used as photocatalysts due to their ultrathin and high specific surface area.[18−20] InS as an In-based semiconductor, which belongs to group III−VI, can be used as a typical representative.[21,22] In and S atoms are arranged in a S−In−S structure, and each layer is connected by van der Waals forces. It has excellent light response characteristics, and the indirect band gap of a monolayer is 2.73 eV.[23] In order to easily fabricate high-efficiency semiconductor catalysts, it is considered to use InS monolayer as a substrate, and another isomorphic semiconductor is selected to construct a heterostructure together. As another III−VI chalcogenide, GaSe also shows great potential in the field of optoelectronics.[24−26] What's more important is that InS and GaSe have been successfully synthesized in experiments. Single crystal GaSe can be prepared on a single crystal silicon substrate by the chemical vapor deposition (CVD) or atomic layer deposition (ALD) method.[27,28] Because of the same crystal type and similar lattice parameters, GaSe and InS nanosheets
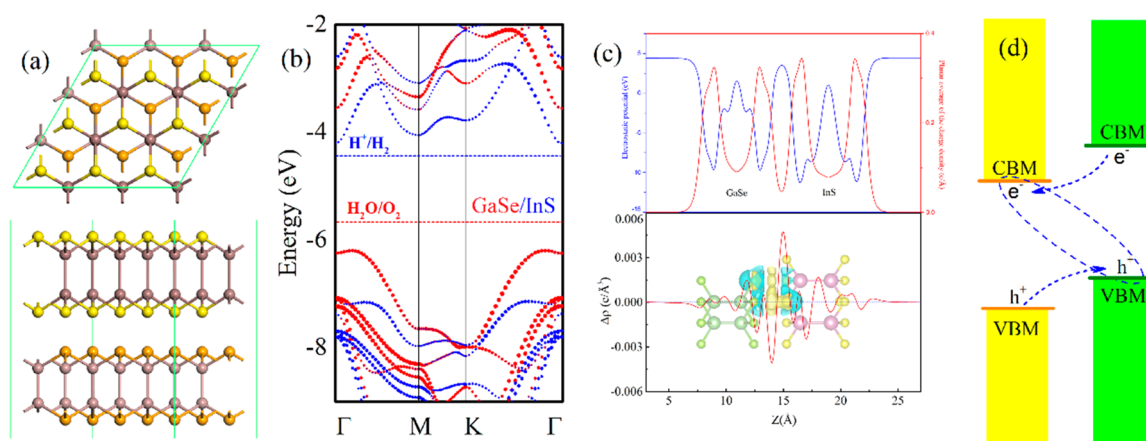
Figure 1. (a) Top and side views of the optimized geometric structures, (b) band structures, (c) effective electrostatic potential profile and planar average charge density difference along the Z-direction of the GaSe/InS heterostructure, and (d) schematic diagram of electron and hole transfers and recombination of the type II heterostructure.

can be prepared by replacing the reaction source gas and forming films by CVD twice. Hence, the GaSe/InS heterostructure is easier to be fabricated than other heterostructures. Rawat et al. and Chen et al. have studied the basic optoelectronic properties of the GaSe/InS heterostructure and verified that the GaSe/InS heterostructure is a potential visible light water splitting photocatalyst. However, there are some deficiencies in the analysis of the free energy change of each step of the water splitting reaction and the exciton binding energy of the GaSe/InS heterostructure.[29,30] Moreover, scientists have also conducted related studies on the isomorphic heterostructure. Fan et al. have regulated the concentration of vanadium dopant in monolayer WSe_2 by CVD and vertically stacked on the $SnSe_2$ layer, demonstrating the tunable multifunctional quantum tunneling diode.[31]

In addition to the method of synthesizing heterostructures, chemical doping is often used as one of the effective ways to improve the efficiency of H_2 production, which could introduce surface defects to better separate electron hole pairs.[32,33] It is proved that doping metal atoms can greatly expand the optical absorption range of semiconductor materials.[34] Different metal atoms have different carrier transport and capture ability, so the effect of photocatalytic performance is also different.[35] Metal doping is not suitable for industrial production because of its high cost, poor stability, and troublesome preparation process. In addition, nonmetallic atom doping can enhance the energy band position of semiconductor materials, narrow the band gap or form a new energy level to capture carriers, and further improve the migration efficiency of photogenerated carriers.[36] Kim et al. have studied the charge transfer mechanism of B-doped C_3N_4/ZnO heterostructure from the Z-scheme to type II, and the photocatalytic hydrogen evolution efficiency is 2.9 times than that of the undoped.[37] In recent years, it has been reported that P atoms are often used to improve the activity of the hydrogen evolution reaction (HER) electrocatalyst. Doping P can reduce the free energy of hydrogen adsorption.[38] P has a kind of gaseous material phosphine, which is a common material for vapor deposition and an excellent candidate for doping in the semiconductor industry. In the preparation of heterostructures, phosphine can be added into the gas source, which can be decomposed into a P atom and H_2 by heating. Based on the above factors, and considering the environ-

mentally friendly and easy access of nonprecious metal elements,[39−42] P, N, and O elements are selected for doping, which can be used as efficient dopants for isomorphous GaSe/InS heterostructure.

In this work, density functional theory (DFT) is used to investigate the structural model, band edge position, and photoelectric properties of isomorphic stacking semiconductors GaSe/InS and P-doped GaSe/InS (P-GaSe/InS) heterostructures. The effect of doping on the water splitting reaction is emphatically discussed. Related electronic properties verify that heterostructures can be used for photocatalytic water splitting reactions. In addition, the different reaction paths of the water splitting reaction are studied. Through the analysis of Gibbs free energy changes in the reaction steps, it is found that GaSe/InS heterostructure can only carry out the overall water splitting after P-doping. The optical properties of the GaSe/InS heterostructure are also improved after P doping. These studies have effectively confirmed that P-GaSe/InS isomorphous heterostructure can be used as a favorable candidate for photocatalyst with excellent performance.

Based on the density functional theory, the Vienna ab initio simulation package (VASP)[43] and the projected augmented wave (PAW)[44] method are used for first-principles calculations. Because the generalized gradient approximation of the Perdew−Burke−Ernzerh (GGA-PBE)[45] function underestimates the band gap, the HSE06 hybrid function method[46] is used to calculate the electronic properties more accurately. At the same time, optical properties such as absorption and reflection are used in combination with the GW approximation[47,48] and the Bethe−Salpeter equation (BSE)[49] and are compared with the GW approximation and random phase approximation (RPA).[50] The effect of van der Waals interactions of heterostructures can be described by the DFT-D3 correction method[51] in Grimme's scheme. Subsequent calculations set the cutoff energy of the plane wave to 400 eV, the energy convergence tolerance to 1×10^{-5} eV, the maximum residual force to 0.03 eV/Å, the maximum displacement of each atom to 0.001 Å, and addition of the 20 Å vacuum zone. In addition, the Brillouin zone was sampled by a Monkhorst−Pack k-point mesh[52] of $4 \times 4 \times 1$.

First, it is necessary to optimize the geometry of GaSe and InS monolayers to understand their structural characteristics and obtain the most stable structure. The lattice parameters of
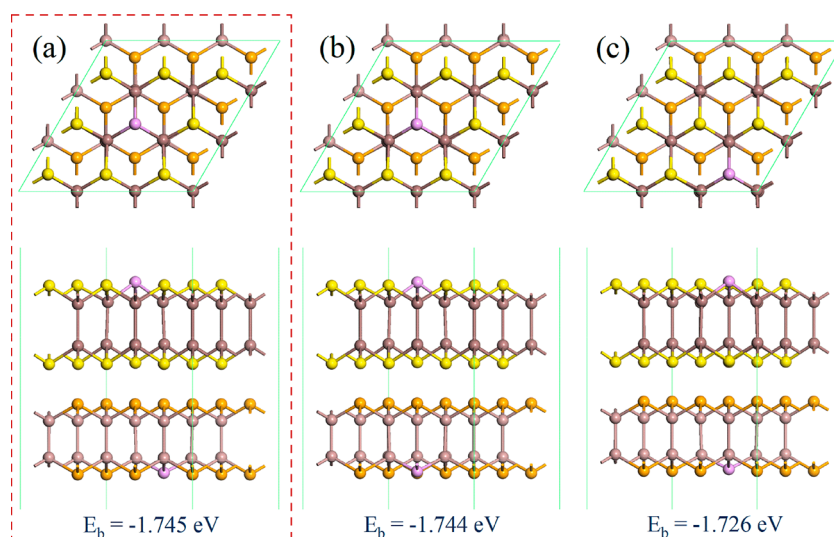
Figure 2. Different optimized geometries of the P-GaSe/InS heterostructures. E_b is marked below the structure.

GaSe and InS monolayers after structural optimization are 3.77 and 3.89 Å, respectively, which are similar to the results of previous studies.[53−55] The symmetry space groups of them are both $P3m1$ (no. 156). The band structures of GaSe and InS monolayers are calculated by the HSE06 functional. As shown in Figure S1, they are both indirect band gap semiconductors with band gaps of 2.90 and 2.73 eV, respectively. Since the lattice parameters of GaSe and InS monolayers are similar, within the allowable range of lattice mismatch, GaSe monolayer with 1 × 1 supercell and InS monolayer with 1 × 1 supercell are stacked into the GaSe/InS heterostructure. The newly combined heterostructure is optimized to obtain a lattice parameter of 3.83 Å, and the corresponding lattice mismatch is calculated to be 3.13%. Considering the element doping in the later stage, it is necessary to expand the heterostructure into a 3 × 3 supercell with the number of 72 atoms, thereby reducing the atomic doping percentage, and the geometry of 3 × 3 GaSe/InS heterostructure is obtained. The stacking structure is shown in Figure 1a. Ga and In atoms are vertically symmetrical. Se and S atoms are correspondingly placed in the hexagonal hole positions of the substrate, which is the most stable stacking pattern of GaSe/InS heterostructures.

Next, the electronic properties of the GaSe/InS heterostructure are further discussed. According to the HSE06 functional calculation, the band structure of the GaSe/InS heterostructure is shown in Figure 1b. The position of VBM is between the Γ and M points, while CBM is located at the Γ point, which shows that GaSe/InS heterostructure is an indirect band gap semiconductor with a band gap of 2.09 eV. In addition, relative to the vacuum energy level, the energy levels of GaSe/InS heterostructure CBM and VBM are −4.12 eV and −6.21 eV, respectively. At the same time, the red and blue lines in Figure 1b have clearly distinguished the contribution of the two materials to the energy band of the GaSe/InS heterostructure, highlighting the typical type II energy band alignment. In the GaSe/InS heterostructure, CBM is contributed by the InS monolayer, while VBM is contributed by the GaSe monolayer. Figure 1c shows the average electrostatic potential and charge density of the GaSe/InS heterostructure. The difference in electronegativity of each element leads to the difference in electrostatic potential and charge density difference on both sides of the GaSe/InS

heterostructure. The charge density difference in the Z direction is defined as

$$\Delta \rho = \rho_{\text{heterostructure}} - \rho_{\text{monolayer1}} - \rho_{\text{monolayer2}} \qquad (1)$$

Among them, $\rho_{\text{heterostructure}}$ represents the charge density of the GaSe/InS heterostructure, and $\rho_{\text{monolayer}}$ refers to the charge density of the GaSe or InS monolayer. The cyan area represents the dissipation of electrons, while the yellow area refers to the accumulation of electrons. It is observed that the available charges dissipate in the GaSe monolayer and gather near the InS monolayer. Bader charge analysis shows that the amount of charge transfer between the GaSe and InS monolayers is about 0.03 e. From the charge density difference, the charge dissipation and aggregation mainly occur in the interface region and the side of S atom. Figure 1d shows a schematic diagram of the transition of photogenerated electrons and holes. The electrons and holes generated by the absorbing energy are located in two different monolayers. The above results show that a certain amount of charge transfer occurs at the interface and surface of the GaSe/InS heterostructure compared with the monolayers, and this charge transfer behavior can further help the separation of photogenerated electrons and holes, thereby effectively improving the photocatalytic efficiency.

Three kinds of nonmetallic elements (P, N, O) are selected for doping. When doping X (X = P, N, O) atoms, consider that there are reactions at the upper and lower interfaces of the GaSe/InS heterostructure, and the doping of one or two X atoms hardly changes the energy band properties of the heterostructure. Therefore, the upper and lower layers of the GaSe/InS heterostructure are doped with a X atom, respectively. The total atom numbers in the GaSe/InS heterostructure are 72. The doping concentration of X is 1/17, which is the ratio of X atoms to Se atoms or S atoms. Thus, the doping percentage is 2.78%. For GaSe/InS heterostructures, it is believed that doping in the middle of the two layers is difficult to adsorb and desorb, and the ALD method can accurately control the preparation and doping of the atomic layer for heterostructure. Based on the above consideration, nine different doping structures are constructed as shown in Figure 2 and Figure S2. The stability of the three doping
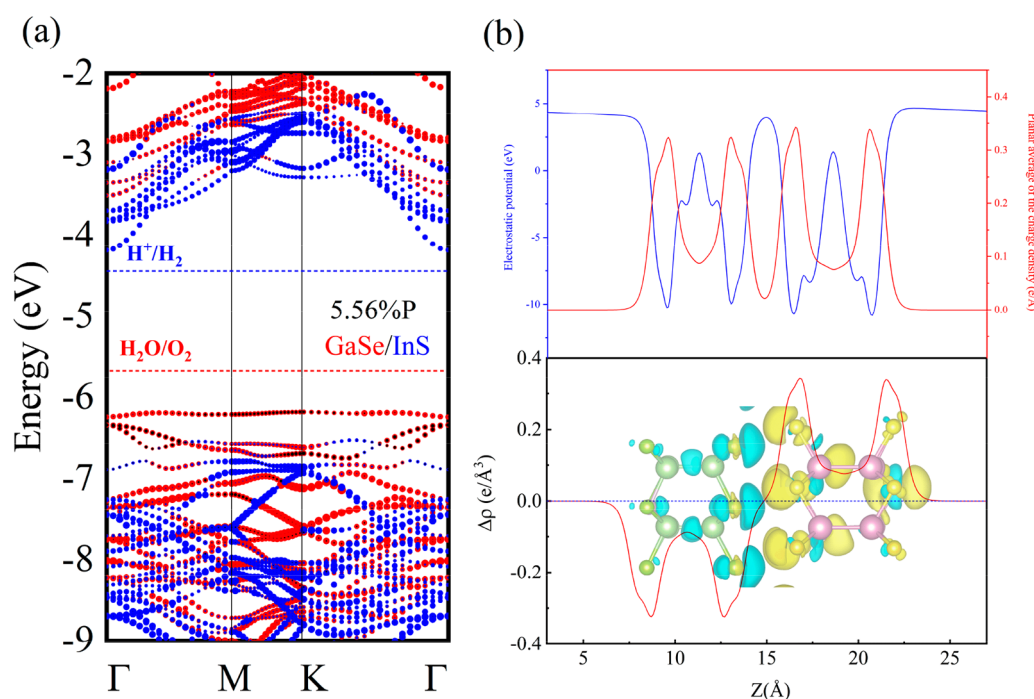
Figure 3. (a) Band structure and (b) effective electrostatic potential profile and planar average charge density difference along the Z-direction of the P-GaSe/InS heterostructure.

structures is calculated and analyzed from the perspective of binding energy (E_b). The E_b calculation formula is as follows:

$$E_b = E_{\text{X-heterostructure}} - E_{\text{X-monolayer1}} - E_{\text{X-monolayer2}} \quad (2)$$

where $E_{\text{X-heterostructure}}$ refers to the energy of the GaSe/InS heterostructure doped with two X atoms, while $E_{\text{X-monolayer}}$ refers to the energy of a monolayer of GaSe or InS doped with one X atom. It can be seen from Figure 2 and Figure S2 that E_b of the first P doping structure is the lowest, which is −1.745 eV, and the stacking pattern is the most stable structure. That is, a P atom replaces the S atom directly below the hexagonal cavity of the GaSe layer, and another P atom replaces the Se atom diagonally next to the hexagonal cavity of the InS layer, which is labeled as the P-GaSe/InS heterostructure. The subsequent performance analysis will apply on the P-GaSe/InS heterostructure. The band structure of P-GaSe/InS heterostructure is calculated by the HSE06 functional and shown in Figure 3a. The red and blue lines are still the bands provided by the P-GaSe monolayer and the P-InS monolayer. The only difference is the black band provided by the doping P. The P-GaSe/InS heterostructure also exhibits a type II energy band arrangement structure. It can be found that the energy band provided by P is mainly distributed at VBM, but the proportion is very small. In order to distinguish the different elements in the energy band structure diagram obviously, the result is shown in Figure 3a that the proportion of the P element in the energy band is increased by three times; that is, the proportion of other elements is 1 and P is 3. The band gap of the P-GaSe/InS heterostructure is 2.05 eV. Carrier mobility is also one of the most important factors for determining an outstanding photocatalyst. The effective mass is negatively correlated with the carrier mobility. Therefore, the effective mass of electrons (m_e) and the effective mass of holes (m_h) of the P-GaSe/InS heterostructure are calculated. The m_e and m_h are $0.1056m_0$ and $-0.7612m_0$, respectively, which highlights the advantage of the P-GaSe/InS heterostructure in carrier

mobility. Figure 3b shows the planar average electrostatic potential and charge density difference of the P-GaSe/InS heterostructure. The calculation method of the charge density difference is consistent with the above method. Compared with the GaSe/InS heterostructure, it is found that the trend of electrostatic potential and charge density after doping P atoms is the same, but the value changes slightly. The charge density difference of the P-GaSe/InS heterostructure shows a very obvious boundary between the cyan region and yellow regions. The P-GaSe layer shows the dissipation of charge, and the P-InS layer shows the charge accumulation. This result can accurately determine that the charge is transferred from the P-GaSe layer to the P-InS layer. The profile also reflects that the electron hole pair separation of the P-GaSe/InS heterostructure is excellent.

Although the band gap and energy band arrangement of the GaSe/InS heterostructure and P-GaSe/InS heterostructure meet the requirements of the photocatalyst, it is necessary to determine whether the band edge position of the heterostructure meets the occurrence of HER and OER. The standard potentials of H^+/H_2 (E_{H^+/H_2}) and H_2O/O_2 (E_{H_2O/O_2})[56,57] with different pH values can be calculated from the standard potentials under acidic conditions at pH = 0 $(E_{H^+/H_2} = -4.44$ eV, $E_{H_2O/O_2} = -5.67$ eV), the formula is as follows:[58]

$$E_{H^+/H_2} = -4.44 + 0.059\,\text{pH} \quad (3a)$$

$$E_{H_2O/O_2} = -5.67 + 0.059\,\text{pH} \quad (3b)$$

In order to carry out the water splitting reaction smoothly, the band edge of the GaSe/InS and P-GaSe/InS heterostructures need to contain E_{H^+/H_2} and E_{H_2O/O_2} under different pH values. If pH = 0, it is necessary to ensure that CBM of the heterostructure is higher than −4.44 eV and VBM is lower than −5.67 eV. Figure 4 is the arrangement diagram of the
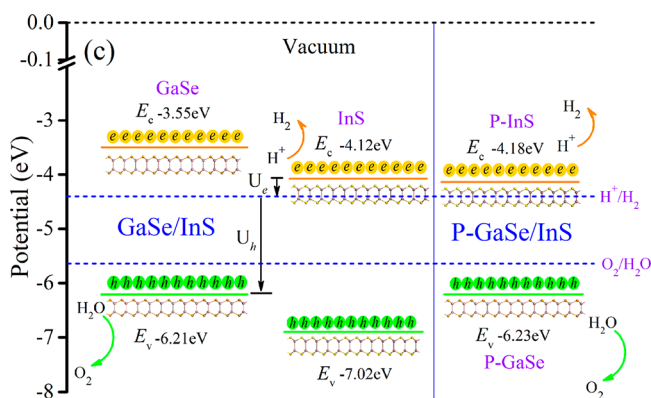
Figure 4. Potential band edge position of the GaSe/InS and P-GaSe/InS heterostructures.

energy band structure of the GaSe/InS and P-GaSe/InS heterostructures. The standard redox potential of the water splitting reaction at pH = 0 has been marked by a blue dotted line. The driving potential for the water splitting reaction is marked by U_e and U_h in Figure 4. The GaSe monolayer and InS chalcogenides are not stable under alkaline conditions but exhibit high stability under acidic conditions. Therefore, the water splitting reaction of the heterostructure under acidic conditions is emphatically discussed. For the GaSe/InS heterostructure, the energy bands are only provided by monolayers of GaSe and InS, so it shows that the two monolayers in the heterostructure provide the band edge position of the energy bands, respectively. It is found that the positions of CBM and VBM of the two heterostructures are slightly changed. Compared with the standard hydrogen electrode (NHE), CBMs of the GaSe/InS heterostructure

and the P-GaSe/InS heterostructure are −4.12 eV and −4.18 eV, while the VBMs are −6.21 eV and −6.23 eV, which meet the water splitting redox potential requirements. In addition, compared with the energy levels of HER and OER, in the GaSe/InS heterostructure, the InS layer performs HER, and because the CBM is provided by the InS layer, electrons are generated here. Similarly, the GaSe layer generates OER. Therefore, theoretically, H_2 is generated in the InS layer, and O_2 is generated in the GaSe layer. The above analysis proves that after P doping, the effect on the energy band of the P-GaSe/InS heterostructure is not significant, and it still maintains as the type II heterostructure and the position of the band edge suggests the possibility of the water splitting reaction.

It is crucial for the study of photocatalyst performance to understand the adsorption of water on the catalyst surface. The above discussion has confirmed that the GaSe/InS and P-GaSe/InS heterostructures are suitable for the water splitting reaction. Next, the reaction process is determined by adsorbing water molecules. The water splitting reaction can be divided into two half reactions. HER: $2H^+ + 2e^- = H_2$ at the cathode and OER: $H_2O = 1/2 O_2 + 2H^+ + 2e^-$ at the anode. OER can be divided into more complex multistep single electron transfer paths as follows:[59,60]
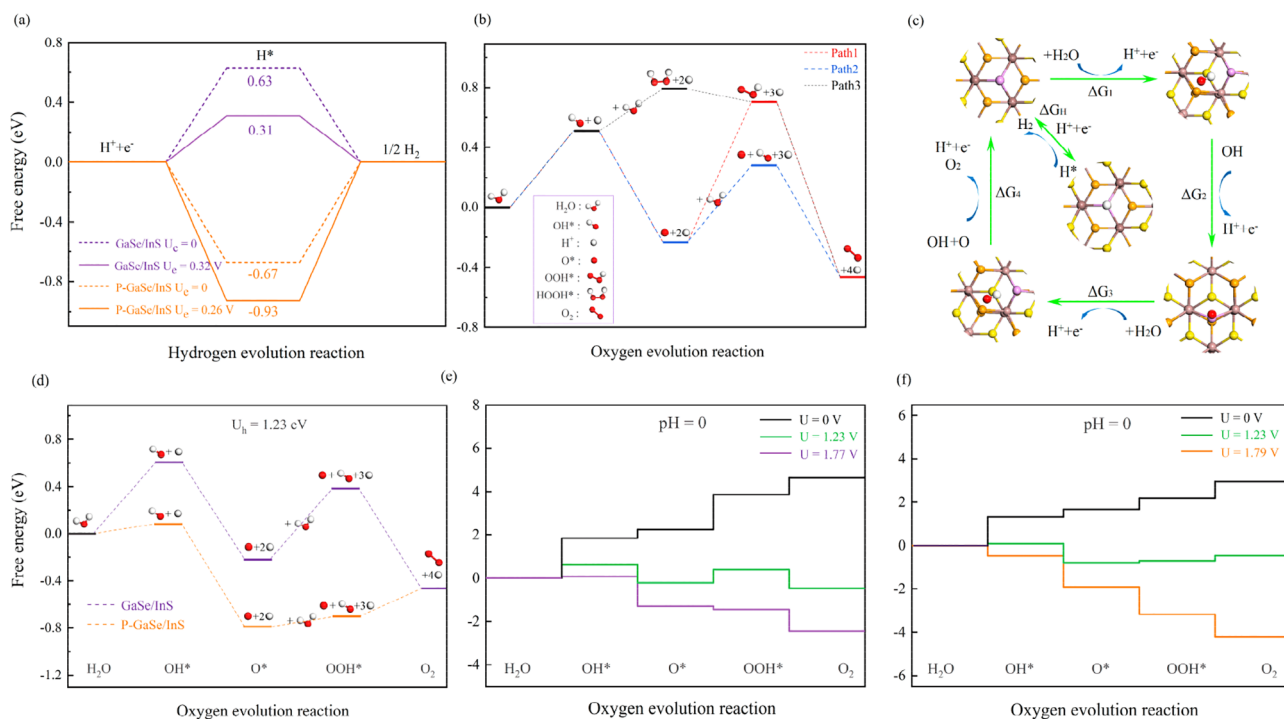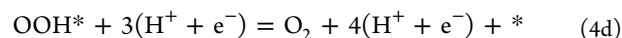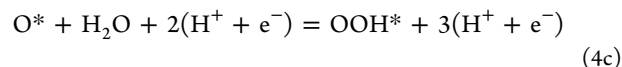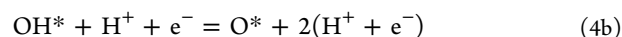
$$H_2O + * = OH* + (H^+ + e^-) \qquad (4a)$$

$$OH* + H^+ + e^- = O* + 2(H^+ + e^-) \qquad (4b)$$

$$O* + H_2O + 2(H^+ + e^-) = OOH* + 3(H^+ + e^-) \qquad (4c)$$

$$OOH* + 3(H^+ + e^-) = O_2 + 4(H^+ + e^-) + * \qquad (4d)$$
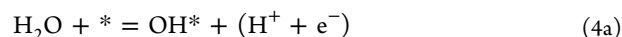

Figure 5. (a) Gibbs free energy (ΔG) diagram of HER occurring on the surface of GaSe/InS and P-GaSe/InS heterostructures. (b) ΔG diagram of three reaction paths in OER (U = 1.23 V). (c) Schematic diagram of the elementary reaction of HER and the path 2 OER process. (d) ΔG diagram of OER under the condition of U = 1.23 V. ΔG diagrams of OER occurring on the surface of (e) GaSe/InS and (f) P-GaSe/InS heterostructures.
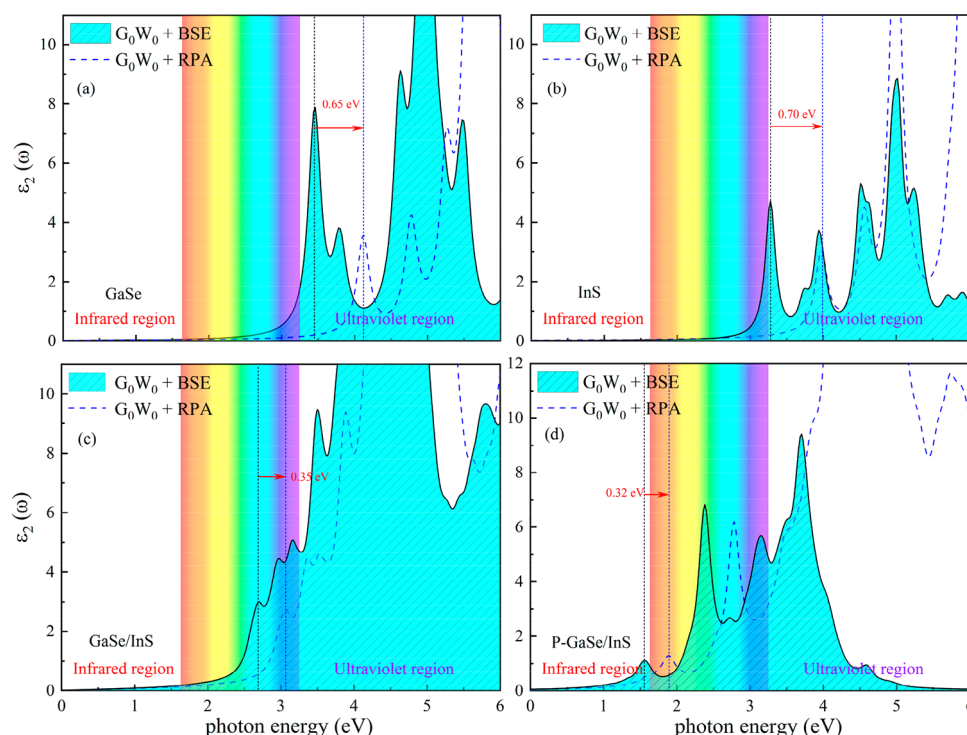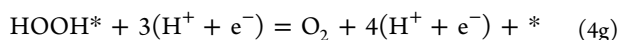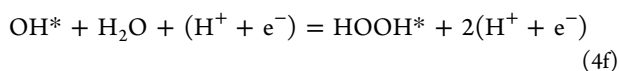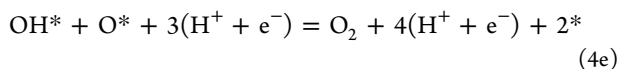
Figure 6. Optical absorption spectra of monolayers (a) GaSe and (b) InS and (c) GaSe/InS and (d) P-GaSe/InS heterostructures.

$$OH* + O* + 3(H^+ + e^-) = O_2 + 4(H^+ + e^-) + 2* \tag{4e}$$

$$OH* + H_2O + (H^+ + e^-) = HOOH* + 2(H^+ + e^-) \tag{4f}$$

$$HOOH* + 3(H^+ + e^-) = O_2 + 4(H^+ + e^-) + * \tag{4g}$$

In this reaction, * refers to the GaSe/InS or P-GaSe/InS heterostructure substrate. According to the above single electron transfer situation, OER can fall into three paths. The flowchart is shown in Figure S3. When the heterostructure adsorbs oxygen and hydrogen atoms, chemical bonds occur. At this time, it is chemical adsorption, and the rest is physical adsorption. The Gibbs free energy (G) corresponding to each step is exhibited, and the change of free energy (ΔG) of each path is calculated in the reaction.

$$\Delta G = \Delta E + \Delta ZPE - T\Delta S - \Delta G_U - \Delta G_{pH} \tag{5}$$

Among them, ΔE and ΔZPE represents the change of total energy and zero point energy of each step. The expression of ZPE is as follows:

$$ZPE = \frac{1}{2}\sum h\nu_i \tag{6}$$

Among them, ν_i is the vibration frequency. At a room temperature of 298.15 K, ΔS is considered to be the entropy contribution, TS can be expressed as

$$TS = k_b T \left[\sum_K \ln\left(\frac{1}{1 - e^{h\nu/k_b T}}\right) + \sum_K \frac{h\nu}{k_b T}\left(\frac{1}{e^{h\nu/k_b T} - 1}\right) + 1 \right] \tag{7}$$

where k_b is the Boltzmann constant, e is the electron charge, and h is Planck's constant. ΔG_U is regarded as the effect of electrode potential U on the reaction, which can be expressed as

$$\Delta G_U = -eU \tag{8}$$

In HER, the value of U is set to the heterostructure CBM position and E_{H_2O/O_2} is the position difference. In OER, it is set as the VBM position of the heterostructure and E_{H^+/H_2}. Again, ΔG_{pH} is viewed as the influence of pH on the reaction. In different reactions, it is calculated in different ways, and the corresponding values in HER and OER can be written as

$$\Delta G_{pH} = -k_b T \ln 10 \times pH \tag{9a}$$

$$\Delta G_{pH} = k_b T \ln 10 \times pH \tag{9b}$$

First, the feasibility of HER is analyzed. Figure 5a shows the free energy diagrams of the GaSe/InS and P-GaSe/InS heterostructures at pH = 0 and different driving potentials. For the GaSe/InS heterostructure, U = 0.32 V, while for the P-GaSe/InS heterostructure, U = 0.26 V. It can be concluded that ΔG of the HER reaction is greater than 0 when U = 0 V and U = 0.32 V without doping. Theoretically, the occurrence of HER is very difficult, which seriously hinders the photocatalytic reaction, so this is also the main reason for applying doping. The ΔG of the doped GaSe/InS heterostructure will be negative, which means that HER could proceed spontaneously. Then OER is discussed. The three possible OER paths of the P-GaSe/InS heterostructure are screened, and the conditions are set as pH = 0, U = 1.23 V equilibrium potential. ΔG of each step in different paths are calculated, as shown in Figure 5b. The small molecule model marked with adsorption in the figure is used to visualize the reaction steps. According to G, path 2 has the lowest overall G and OER is the easiest to proceed. Therefore, path 2 is selected

to analyze ΔG of OER under acidic conditions and different driving potentials. Taking path 2 of OER and HER as examples, Figure 5c gives a detailed flowchart of the P-GaSe/InS heterostructure adsorbing small molecules. Since GaSe and InS are more stable under acidic conditions, the condition of pH = 0 has been studied in detail. Since the catalyst that meets the photocatalytic conditions has an OER driving potential of at least 1.23 V, for OER in Figure 5d, the four step ΔG of the GaSe/InS and P-GaSe/InS heterostructures are compared under the conditions of $U = 1.23$ V and pH = 0. The G after doping is significantly reduced, which is conducive to the reaction. Figure 5e,f displays the ΔG diagram of the heterostructure at pH = 0 and different driving forces for OER. When $U = 0$ V, G of each step of the heterostructure increases, which means OER needs to overcome a large energy barrier. At a driving potential of 1.77 V, the first step G of the GaSe/InS heterostructure goes up slightly, while the rest of the steps decrease, indicating that OER is relatively reluctant. When $U = 1.79$ V, G of all the steps involved in the reaction is reduced, which implies that the OER process can continue in thermodynamics. It can be seen that doping promotes the smooth progress of HER and OER for the P-GaSe/InS heterostructure.

It is inevitable to consider the optical absorption performance of the photocatalyst. The exciton binding energy is related to the separation of photogenerated carriers. The calculation method can be carried out according to the Wannier−Mott model of two-dimensional materials or related calculation formulas.[61,62] However, Figure 6 exhibits the calculation results of optical properties using G_0W_0+BSE and G_0W_0+RPA in this paper. The G_0W_0+RPA calculation does not consider the influence of exciton binding energy on optical absorption, while the G_0W_0+BSE calculation results are more accurate because it refers to the optical absorption capacity corrected by BSE exciton. The purpose of comparing whether to add BSE exciton binding energy correction is to compare their exciton binding energy, which affects the recombination of electrons and holes.[63,64] The greater the energy, the easier it is for electrons and holes to recombine, which is negative for photocatalysts. The distance between the light absorption peaks calculated by the two methods is the material exciton binding energy. The blue dotted line in Figure 6 shows the light absorption peak given by the G_0W_0+RPA method, the cyan shaded area shows the light absorption peak calculated by the G_0W_0+BSE method, and the red arrow is used to mark the exciton binding energy. The exciton binding energy of heterostructure is much smaller than that of the monolayer, and the exciton binding energy of the doped P-GaSe/InS heterostructure is the smallest, 0.32 eV, which also suggests that electrons and holes are the least likely to recombine, and the catalyst performance is more outstanding. In Figure 6, there is no absorption peak in the visible region for the monolayers of GaSe and InS, but there is an obvious absorption peak in the visible region for the GaSe/InS heterostructure. The optical absorption range becomes larger, which indicates that the optical absorption ability of the GaSe/InS heterostructure has been significantly improved. For the P-GaSe/InS heterostructure, a higher peak appears in the visible region, and the optical absorption capacity is also strengthened for the undoped heterostructure. The photocatalytic performance of the catalyst can also be judged by studying the solar-to-hydrogen (STH) efficiency. STH efficiency can be approximately estimated by the following expression:[65,66]

$$\eta_{STH} = \frac{\Delta G \int_{E_g}^{\infty} \frac{P(\hbar\omega)d(\hbar\omega)}{\hbar\omega}}{\int_0^{\infty} P(\hbar\omega)d(\hbar\omega)} \qquad (10)$$

Among them, ΔG is approximately regarded as a free energy difference of 1.23 eV, $P(\hbar\omega)$ refers to the solar flux of AM1.5, and E_g is equivalent to the band gap corresponding to the photon energy of water splitting. By calculation, the STHs efficiency of the GaSe/InS heterostructure and the P-GaSe/InS heterostructure are 15.25% and 16.36%, respectively, which manifests excellent STH performance of the GaSe/InS and P-GaSe/InS heterostructures.

Density functional theory is used to study the electronic structure and optical properties of the GaSe/InS and P-doped GaSe/InS heterostructures. The band gaps of the GaSe/InS and P-GaSe/InS heterostructures are 2.09 and 2.05 eV, respectively. The energy band arrangement of type II promotes the separation of electrons and holes in the heterostructure and can effectively enhance the photocatalytic efficiency. The band gap and edge position of the heterostructure meet the requirements of the water splitting reaction. By analyzing the free energy changes of HER and OER, it is found that the P-doped GaSe/InS heterostructure has an overall spontaneous water splitting at pH = 0. Finally, the exciton binding energy of the P-GaSe/InS heterostructure is 0.32 eV, and it is verified that the P-doped GaSe/InS heterostructure has more marvelous optical absorption performance.

■ ASSOCIATED CONTENT

Ⓢ Supporting Information

The Supporting Information is available free of charge at https://pubs.acs.org/doi/10.1021/acs.jpclett.1c02040.

Figure S1, band structures of GaSe and InS; Figure S2, different optimized geometries of N-GaSe/InS heterostructures and O-GaSe/InS heterostructures; and Figure S3, schematic diagram of the elementary reaction of path 1, path 2, and path 3 of the OER process (PDF)

■ AUTHOR INFORMATION

Corresponding Author

C. He − *State Key Laboratory for Mechanical Behavior of Materials, School of Materials Science and Engineering, Xi'an Jiaotong University, Xi'an 710049, China;* ⓘ orcid.org/0000-0002-6612-5346; Email: hecheng@mail.xjtu.edu.cn

Authors

W. X. Zhang − *School of Materials Science and Engineering, Chang'an University, Xi'an 710064, China;* ⓘ orcid.org/0000-0002-9327-5761

Y. Yin − *School of Materials Science and Engineering, Chang'an University, Xi'an 710064, China*

Complete contact information is available at:
https://pubs.acs.org/10.1021/acs.jpclett.1c02040

Notes

The authors declare no competing financial interest.

■ REFERENCES

(1) Zhang, Y.; Xie, W.; Ma, J.; Chen, L.; Chen, C.; Zhang, X.; Shao, M. Active Facet Determination of Layered Double Hydroxide for Oxygen Evolution Reaction. *J. Energy Chem.* **2021**, *60*, 127−134.

(2) Shukla, S.; Bayomy, A. M.; Antoun, S.; Mwesigye, A.; Leong, W. H.; Dworkin, S. B. Performance Characterization of Novel Caisson-Based Thermal Storage for Ground Source Heat Pumps. *Renewable Energy* **2021**, *174*, 43−54.

(3) Liu, Y.; Li, X.; He, H.; Yang, S.; Jia, G.; Liu, S. CoP Imbedded g-C_3N_4 Heterojunctions for Highly Efficient Photo, Electro and Photoelectrochemical Water Splitting. *J. Colloid Interface Sci.* **2021**, *599*, 23−33.

(4) Ju, L.; Liu, P.; Yang, Y.; Shi, L.; Yang, G.; Sun, L. Tuning the Photocatalytic Water-Splitting Performance with the Adjustment of Diameter in an Armchair WSSe Nanotube. *J. Energy Chem.* **2021**, *61*, 228−235.

(5) Yang, X.; Sun, H.; Li, G.; An, T.; Choi, W. Fouling of TiO_2 Induced by Natural Organic Matters during Photocatalytic Water Treatment: Mechanisms and Regeneration Strategy. *Appl. Catal., B* **2021**, *294*, 120252.

(6) Verma, S.; Younis, S. A.; Kim, K. H.; Dong, F. Anisotropic ZnO Nanostructures and their Nanocomposites as an Advanced Platform for Photocatalytic Remediation. *J. Hazard. Mater.* **2021**, *415*, 125651.

(7) Yu, F.; Tian, F.; Zou, H.; Ye, Z.; Peng, C.; Huang, J.; Zheng, Y.; Zhang, Y.; Yang, Y.; Wei, X.; Gao, B. ZnO/Biochar Nanocomposites Via Solvent Free Ball Milling for Enhanced Adsorption and Photocatalytic Degradation of Methylene Blue. *J. Hazard. Mater.* **2021**, *415*, 125511.

(8) Li, W.; Jin, L.; Gao, F.; Wan, H.; Pu, Y.; Wei, X.; Chen, C.; Zou, W.; Zhu, C.; Dong, L. Advantageous Roles of Phosphate Decorated Octahedral CeO_2 {111}/g-C_3N_4 in Boosting Photocatalytic CO_2 Reduction: Charge Transfer Bridge and Lewis Basic Site. *Appl. Catal., B* **2021**, *294*, 120257.

(9) Wang, Y.; Li, X.; Lei, W.; Zhu, B.; Yang, J. Novel Carbon Quantum Dot Modified g-C_3N_4 Nanotubes on Carbon Cloth for Efficient Degradation of Ciprofloxacin. *Appl. Surf. Sci.* **2021**, *559*, 149967.

(10) Chatterjee, K.; Dos Reis, R.; Harada, J. K.; Mathiesen, J. K.; Bueno, S. L. A.; Jensen, K. M. O.; Rondinelli, J. M.; Dravid, V.; Skrabalak, S. E. Durable Multimetal Oxychloride Intergrowths for Visible Light-Driven Water Splitting. *Chem. Mater.* **2021**, *33* (1), 347−358.

(11) Zhao, T.; Chen, J.; Wang, X.; Yao, M. Ab-Initio Insights into Electronic Structures, Optical and Photocatalytic Properties of Janus WXY (X/Y = O, S, Se and Te). *Appl. Surf. Sci.* **2021**, *545*, 148968.

(12) Zhang, C.; Liu, B.; Li, W.; Liu, X.; Wang, K.; Deng, Y.; Guo, Z.; Lv, Z. A Well-Designed Honeycomb Co_3O_4@CdS Photocatalyst Derived from Cobalt Foam for High-Efficiency Visible-Light H_2 Evolution. *J. Mater. Chem. A* **2021**, *9* (19), 11665−11673.

(13) Chong, B.; Zhu, W.; Hou, X. Epitaxial Heterostructure of CdSe/TiO_2 Nanotube Arrays with Pedot as a Hole Transfer Layer for Photoelectrochemical Hydrogen Evolution. *J. Mater. Chem. A* **2017**, *5* (13), 6233−6244.

(14) Roge, V.; Bahlawane, N.; Lamblin, G.; Fechete, I.; Garin, F.; Dinia, A.; Lenoble, D. Improvement of the Photocatalytic Degradation Property of Atomic Layer Deposited ZnO Thin Films: The Interplay between Film Properties and Functional Performances. *J. Mater. Chem. A* **2015**, *3* (21), 11453−11461.

(15) Gogoi, D.; Shah, A. K.; Qureshi, M.; Golder, A. K.; Peela, N. R. Silver Grafted Graphitic-Carbon Nitride Ternary Heterojunction Ag/ gC_3N_4(Urea)-g-C_3N_4(Thiourea) with Efficient Charge Transfer for Enhanced Visible-Light Photocatalytic Green H_2 Production. *Appl. Surf. Sci.* **2021**, *558*, 149900.

(16) Omar, A. M. A.; Hassen, A.; Metwalli, O. I.; Saber, M. R.; Mohamed, S. R. E.; Khalil, A. S. G. Construction of 2D Layered TiO_2@MoS_2 Heterostructure for Efficient Adsorption and Photodegradation of Organic Dyes. *Nanotechnology* **2021**, *32* (33), 335605.

(17) Zhang, T.; Meng, F.; Cheng, Y.; Dewangan, N.; Ho, G. W.; Kawi, S. Z-scheme Transition Metal Bridge of Co_9S_8/Cd/CdS Tubular Heterostructure for Enhanced Photocatalytic Hydrogen Evolution. *Appl. Catal., B* **2021**, *286*, 119853.

(18) Su, T.; Shao, Q.; Qin, Z.; Guo, Z.; Wu, Z. Role of Interfaces in Two-Dimensional Photocatalyst for Water Splitting. *ACS Catal.* **2018**, *8* (3), 2253−2276.

(19) Zhu, Y. L.; Yuan, J. H.; Song, Y. Q.; Wang, S.; Xue, K. H.; Xu, M.; Cheng, X. M.; Miao, X. S. Two-Dimensional Silicon Chalcogenides with High Carrier Mobility for Photocatalytic Water Splitting. *J. Mater. Sci.* **2019**, *54* (17), 11485−11496.

(20) Naseri, M.; Bafekry, A.; Faraji, M.; Hoat, D. M.; Fadlallah, M. M.; Ghergherehchi, M.; Sabbaghi, N.; Gogova, D. Two-Dimensional Buckled Tetragonal Cadmium Chalcogenides Including CdS, CdSe, and CdTe Monolayers as Photo-Catalysts for Water Splitting. *Phys. Chem. Chem. Phys.* **2021**, *23* (21), 12226−12232.

(21) Zhang, Y.; Sa, B.; Miao, N.; Zhou, J.; Sun, Z. Computational Mining of Janus Sc_2C- Based Mxenes for Spintronic, Photocatalytic, and Solar Cell Applications. *J. Mater. Chem. A* **2021**, *9* (17), 10882− 10892.

(22) Kang, D.; Kong, X.; Michaud-Rioux, V.; Chen, Y. C.; Mi, Z.; Guo, H. Electronic Structure of Aqueous Two-Dimensional Photocatalyst. *npj Comput. Mater.* **2021**, *7*, 47.

(23) Zhao, Y.; He, Y.; Zhang, M.; Shi, J. First-principles Study on the Photocatalytic Hydrogen Production of a Novel Two-dimensional Zr_2CO_2/InS Heterostructure. *J. Inorg. Mater.* **2020**, *35* (9), 993−998.

(24) Zappia, M. I.; Bianca, G.; Bellani, S.; Serri, M.; Najafi, L.; Oropesa-Nunez, R.; Martin-Garcia, B.; Bousa, D.; Sedmidubsky, D.; Pellegrini, V.; Sofer, Z.; Cupolillo, A.; Bonaccorso, F. Solution-Processed GaSe Nanoflake-Based Films for Photoelectrochemical Water Splitting and Photoelectrochemical-Type Photodetectors. *Adv. Funct. Mater.* **2020**, *30* (10), 1909572.

(25) Obeid, M. M.; Bafekry, A.; Ur Rehman, S.; Nguyen, C. V. A Type-II GaSe/HfS_2 Van Der Waals Heterostructure as Promising Photocatalyst with High Carrier Mobility. *Appl. Surf. Sci.* **2020**, *534*, 147607.

(26) Wang, B.; Wang, G.; Yuan, H.; Kuang, A.; Chang, J.; Huang, Y.; Chen, H. Strain-Tunable Electronic and Optical Properties in Two Dimensional GaSe/g-C_3N_4 Van Der Waals Heterojunction as Photocatalyst for Water Splitting. *Phys. E* **2020**, *118*, 113896.

(27) Kumar, A. S.; Wang, M.; Li, Y.; Fujita, R.; Gao, X. P. A. Interfacial Charge Transfer and Gate-Induced Hysteresis in Monochalcogenide InSe/GaSe Heterostructures. *ACS Appl. Mater. Interfaces* **2020**, *12* (41), 46854−46861.

(28) Xu, K.; Yin, L.; Huang, Y.; Shifa, T. A.; Chu, J.; Wang, F.; Cheng, R.; Wang, Z.; He, J. Synthesis, Properties and Applications of 2D Layered (MXVI)-X-III (M = Ga, In; X = S, Se, Te) Materials. *Nanoscale* **2016**, *8* (38), 16802−16818.

(29) Rawat, A.; Ahammed, R.; Dimple; Jena, N.; Mohanta, M. K.; De Sarkar, A. Solar Energy Harvesting in Type II Van Der Waals Heterostructures of Semiconducting Group III Monochalcogenide Monolayers. *J. Phys. Chem. C* **2019**, *123* (20), 12666−12675.

(30) Chen, J.; He, X.; Sa, B.; Zhou, J.; Xu, C.; Wen, C.; Sun, Z. III-VI Van Der Waals Heterostructures for Sustainable Energy Related Applications. *Nanoscale* **2019**, *11* (13), 6431−6444.

(31) Fan, S.; Yun, S. J.; Yu, W. J.; Lee, Y. H. Tailoring Quantum Tunneling in a Vanadium-Doped WSe_2/$SnSe_2$ Heterostructure. *Adv. Sci.* **2020**, *7* (3), 1902751.

(32) Goswami, T.; Yadav, D. K.; Bhatt, H.; Kaur, G.; Shukla, A.; Babu, K. J.; Ghosh, H. N. Defect-Mediated Slow Carrier Recombination and Broad Photoluminescence in Non-Metal-Doped $ZnIn_2S_4$ Nanosheets for Enhanced Photocatalytic Activity. *J. Phys. Chem. Lett.* **2021**, *12* (20), 5000−5008.

(33) Shyamal, S.; Dutta, S. K.; Pradhan, N. Doping Iron in CsPbBr$_3$ Perovskite Nanocrystals for Efficient and Product Selective CO$_2$ Reduction. *J. Phys. Chem. Lett.* **2019**, *10* (24), 7965−7969.

(34) Sutar, S.; Chiappe, D.; Nuytten, T.; Conard, T.; Asselberghs, I.; Lin, D.; Radu, I. Spin-on-Diffusants for Doping in Transition Metal Dichalcogenide Semiconductors. *Appl. Phys. Lett.* **2019**, *114* (21), 212102.

(35) Yang, L.; Wu, M.; Yao, K. Transition-Metal-Doped Group-IV Monochalcogenides: a Combination of Two-Dimensional Triferroics and Diluted Magnetic Semiconductors. *Nanotechnology* **2018**, *29* (21), 215703.

(36) Su, Y.; Xiong, X.; Wang, X.; Song, K.; Zhou, Y.; Liu, Q.; Qian, P. Theoretical Study on Improving the Catalytic Activity of a Tungsten Carbide Surface for Hydrogen Evolution by Nonmetallic Doping. *Catalysts* **2020**, *10* (11), 1272.

(37) Kim, D.; Yong, K. Boron Doping Induced Charge Transfer Switchin of a C$_3$N$_4$/ZnO Photocatalyst from Z-Scheme to Type II to Enhance Photocatalytic Hydrogen Production. *Appl. Catal., B* **2021**, *282*, 119538.

(38) Zhao, Q.; Qian, Q.; Zhang, B.; Zhang, X. Promoting the Electrocatalytic Activity of Platinum Film for Hydrogen Evolution Reaction by Phosphorus Doping. *Mater. Chem. Phys.* **2021**, *263*, 124412.

(39) Huang, Y.; Li, J.; Du, P.; Lu, X. Rational Design of Copper Encapsulated within Nitrogen-Doped Carbon Core-Shell Nanosphere for Efficiently Photocatalytic Peroxymonosulfate Activation. *J. Colloid Interface Sci.* **2021**, *597*, 206−214.

(40) Wang, L.; Du, D.; Zhang, B.; Xie, S.; Zhang, Q.; Wang, H.; Wang, Y. Solar Energy-Driven C-H Activation of Methanol for Direct C-C Coupling to Ethylene Glycol with High Stability by Nitrogen Doped Tantalum Oxide. *Chin. J. Catal.* **2021**, *42* (9), 1459−1467.

(41) Guo, C.; Li, L.; Chen, F.; Ning, J.; Zhong, Y.; Hu, Y. One-Step Phosphorization Preparation of Gradient-P-Doped CdS/CoP Hybrid Nanorods Having Multiple Channel Charge Separation for Photocatalytic Reduction of Water. *J. Colloid Interface Sci.* **2021**, *596*, 431−441.

(42) Chava, R. K.; Son, N.; Kang, M. Controllable Oxygen Doping and Sulfur Vacancies in One Dimensional CdS Nanorods for Boosted Hydrogen Evolution Reaction. *J. Alloys Compd.* **2021**, *873*, 159797.

(43) Kresse, G.; Furthmuller, J. Efficient Iterative Schemes for Ab Initio Total-Energy Calculations Using a Plane-Wave Basis Set. *Phys. Rev. B: Condens. Matter Mater. Phys.* **1996**, *54* (16), 11169−86.

(44) Blochl, P. E. Projector Augmented-Wave Method. *Phys. Rev. B: Condens. Matter Mater. Phys.* **1994**, *50* (24), 17953−79.

(45) Perdew, J. P.; Burke, K.; Ernzerhof, M. Generalized Gradient Approximation Made Simple. *Phys. Rev. Lett.* **1996**, *77* (18), 3865−8.

(46) Heyd, J.; Scuseria, G. E.; Ernzerhof, M. Hybrid Functionals Based on a Screened Coulomb Potential (vol 118, pg 8207, 2003). *J. Chem. Phys.* **2006**, *124* (21), 219906.

(47) Umari, P.; Stenuit, G.; Baroni, S. Optimal Representation of the Polarization Propagator for Large-Scale GW Calculations. *Phys. Rev. B: Condens. Matter Mater. Phys.* **2009**, *79* (20), 201104.

(48) Umari, P.; Stenuit, G.; Baroni, S. GW Quasiparticle Spectra From Occupied States Only. *Phys. Rev. B: Condens. Matter Mater. Phys.* **2010**, *81* (11), 115104.

(49) Rohlfing, M.; Louie, S. G. Electron-Hole Excitations in Semiconductors and Insulators. *Phys. Rev. Lett.* **1998**, *81* (11), 2312−15.

(50) Providencia, J. d. A Simplified Version of the Random-Phase Approximation and the Problem of the Correlation Energy of a Many Fermion System. *Port. Phys.* **1969**, *5* (4), 125−38.

(51) Grimme, S. Semiempirical GGA-Type Density Functional Constructed with a Long-Range Dispersion Correction. *J. Comput. Chem.* **2006**, *27* (15), 1787−99.

(52) Monkhorst, H. J.; Pack, J. D. Special Points for Brillouin-Zone Integrations. *Phys. Rev. B. (Solid State)* **1976**, *13* (12), 5188−92.

(53) Yao, H.; Zhang, C.; Wang, Q.; Li, J.; Yu, Y.; Xu, F.; Wang, B.; Wei, Y. Tunable Electronic Properties and Band Alignments of Ins-Arsenene Heterostructures Via External Strain and Electric Field. *New J. Chem.* **2021**, *45* (5), 2508−2519.

(54) Abdulraheem, Z.; Jappor, H. R. Tailoring the Electronic and Optical Properties of SnSe$_2$/InS Van Der Waals Heterostructures by the Biaxial Strains. *Phys. Lett. A* **2020**, *384* (35), 126909.

(55) Sutter, P.; French, J. S.; Khosravi Khorashad, L.; Argyropoulos, C.; Sutter, E. Optoelectronics and Nanophotonics of Vapor-Liquid-Solid Grown GaSe van der Waals Nanoribbons. *Nano Lett.* **2021**, *21* (10), 4335−4342.

(56) Li, Q. H.; Ding, Y. F.; He, P. B.; Zeng, R.; Wan, Q.; Cai, M. Q. Transition of the Type of Band Alignments for All-Inorganic Perovskite Van Der Waals Heterostructures CsSnBr$_3$/WS$_{2(1-x)}$Se$_{2x}$. *J. Phys. Chem. Lett.* **2021**, *12* (15), 3809−3818.

(57) Yu, T.; Wang, C.; Yan, X.; Yang, G.; Schwingenschlogl, U. Anisotropic Janus SiP$_2$ Monolayer as a Photocatalyst for Water Splitting. *J. Phys. Chem. Lett.* **2021**, *12* (9), 2464−2470.

(58) Zhuang, H. L.; Hennig, R. G. Single-Layer Group-III Monochalcogenide Photocatalysts for Water Splitting. *Chem. Mater.* **2013**, *25* (15), 3232−3238.

(59) Rossmeisl, J.; Qu, Z. W.; Zhu, H.; Kroes, G. J.; Norskov, J. K. Electrolysis of Water on Oxide Surfaces. *J. Electroanal. Chem.* **2007**, *607* (1−2), 83−9.

(60) Lin, S.; Ye, X.; Gao, X.; Huang, J. Mechanistic Insight into the Water Photooxidation on Pure and Sulfur-Doped g-C$_3$N$_4$ Photocatalysts from DFT Calculations with Dispersion Corrections. *J. Mol. Catal. A: Chem.* **2015**, *406*, 137−144.

(61) Mohanta, M. K.; Rawat, A.; Jena, N.; Dimple; Ahammed, R.; De Sarkar, A. Interfacing Boron Monophosphide with Molybdenum Disulfide for an Ultrahigh Performance in Thermoelectrics, Two-Dimensional Excitonic Solar Cells, and nanopiezotronics. *ACS Appl. Mater. Interfaces* **2020**, *12* (2), 3114−3126.

(62) Yang, H.; Ma, Y.; Zhang, S.; Jin, H.; Huang, B.; Dai, Y. GeSe@ SnS: Stacked Janus Structures for Overall Water Splitting. *J. Mater. Chem. A* **2019**, *7* (19), 12060−12067.

(63) Hao, Q. D.; Luo, Y.; Zeng, Z. Y.; Chen, X. R.; Chen, Q. F. Quasiparticle Band Structures and Optical Properties of Monolayer ZrNX (X═Cl, Br, I) under Exciton Effect. *Solid State Commun.* **2020**, *322*, 114049.

(64) Jain, M.; Gill, D.; Bhumla, P.; Basera, P.; Bhattacharya, S. Theoretical Insights to Excitonic Effect in Lead Bromide Perovskites. *Appl. Phys. Lett.* **2021**, *118* (19), 192103.

(65) Dotan, H.; Mathews, N.; Hisatomi, T.; Graetzel, M.; Rothschild, A. On the Solar to Hydrogen Conversion Efficiency of Photoelectrodes for Water Splitting. *J. Phys. Chem. Lett.* **2014**, *5* (19), 3330−3334.

(66) Fu, X. Y.; Wei, Z. Q.; Xu, S.; Lin, X.; Hou, S.; Xiao, F. X. Maneuvering Intrinsic Instability of Metal Nanoclusters for Boosted Solar-Powered Hydrogen Production. *J. Phys. Chem. Lett.* **2020**, *11* (21), 9138−9143.